

# Far Ultraviolet Spectra of a Non-Radiative Shock Wave in the Cygnus Loop<sup>1</sup>

John C. Raymond<sup>2</sup>

Parviz Ghavamian<sup>3</sup>

Ravi Sankrit<sup>4</sup>

William P. Blair<sup>4</sup>  
and

Salvador Curiel<sup>5</sup>

## ABSTRACT

Spatial and spectral profiles of O VI emission behind a shock wave on the northern edge of the Cygnus Loop were obtained with the FUSE satellite. The velocity width of the narrowest O VI profile places a tight constraint on the electron-ion and ion-ion thermal equilibration in this 350 km s<sup>-1</sup> collisionless shock. Unlike faster shocks in SN1006 and in the heliosphere, this shock brings oxygen ions and protons to within a factor of 2.5 of the same temperature. Comparison with other shocks suggests that shock speed, rather than Alfvén Mach number, may control the degree of thermal equilibration.

We combine the O VI observations with a low resolution far UV spectrum from HUT, an H $\alpha$  image and ROSAT PSPC X-ray data to constrain the pre-shock density and the structure along the line-of-sight. As part of this effort, we model the effects of resonance scattering of O VI photons within the shocked gas and compute time-dependent ionization models of the X-ray emissivity. Resonance scattering affects the O VI intensities at the factor of 2 level, and the soft spectrum of the X-ray rim can be mostly attributed to departures from ionization equilibrium. The pre-shock density is about twice the canonical value for the Cygnus Loop X-ray emitting shocks.

<sup>1</sup>Based on observations made with the NASA-CNES-CSA Far Ultraviolet Spectroscopic Explorer. FUSE is operated for NASA by the Johns Hopkins University under NASA contract NAS5-32985.

<sup>2</sup>Smithsonian Astrophysical Observatory, 60 Garden Street, Cambridge, MA 02138; jraymond@cfa.harvard.edu

<sup>3</sup>Department of Physics and Astronomy, Rutgers University, 136 Freylinghuysen Rd., Piscataway, NJ 08854; parviz@physics.rutgers.edu

<sup>4</sup>Department of Physics and Astronomy, The Johns Hopkins University, 34th & Charles Streets, Baltimore, MD 21218; ravi@pha.jhu.edu, wpb@pha.jhu.edu

<sup>5</sup>Instituto de Astronomía, Universidad Nacional Autónoma de México, Apartado Postal 70-264, 04510 DF, México; suriel@astroscu.unam.mx

*Subject headings:* ISM: supernova remnants – ISM: individual (Cygnus Loop) – shock waves

## 1. Introduction

The Cygnus Loop is a nearby, bright supernova remnant (SNR). Because it is relatively unreddened, it has been extensively studied in the UV with IUE, Voyager, HUT, HST and FUSE (e.g. Raymond et al. 1980; Blair et al. 1991; Long et al. 1992; Vancura et al. 1993; Danforth et al. 2000; Sankrit et al. 2000; Blair et al. 2002; Sankrit & Blair 2002). It is often taken as the prototypical middle-aged SNR, though it was probably formed by a stellar explosion in a relatively low density region of the interstellar medium (ISM) where the progenitor formed a cavity and a dense shell (e.g. Shull et al. 1985; Hester et al. 1994; Levenson et al. 1998; Miyata & Tsunemi 1999). In regions where the blast wave encounters the dense shell, radiative shocks produce bright optical and UV emission. Regions where the blast wave encounters low density gas are seen in X-rays and in the Balmer lines as non-radiative shocks. The distance to the Cygnus Loop is now believed to be 440 pc based on comparison of proper motions and shock speeds (Shull & Hippelien 1991; Blair et al. 1999), as opposed to the canonical estimate of 770 pc.

A non-radiative shock is one that heats plasma to a fairly high temperature, and that has encountered the plasma so recently that the shocked gas has had insufficient time to radiatively cool (McKee & Hollenbach 1980). The optical and UV emission arises from a narrow zone just behind the shock where the elements pass rapidly through successive ionization stages. Collisional excitation causes some of these atoms and ions to emit photons before they are ionized. At visible wavelengths, non-radiative shocks appear as faint filaments of essentially pure Balmer line emission (Chevalier & Raymond 1978; Chevalier, Kirshner & Raymond 1980).

Non-radiative shocks present unique diagnostics for shock speed and for physical processes in shocks, because the emission is produced before Coulomb collisions and radiative cooling erase the signatures of conditions at the shock. Thermal equilibration among different particle species is especially important, as it must be understood for reliable interpretation of electron or ion temperatures in terms of the shock speed (Raymond 2001).

Several non-radiative shocks along the periphery of the Cygnus Loop have been studied in an effort to ob-

tain shock parameters and to investigate the physics of collisionless shocks. The filaments observed were on the western edge (Raymond et al. 1980; Treffers 1981) and the northeastern boundary (Raymond et al. 1983; Fesen & Itoh 1985; Blair et al. 1999; Sankrit et al. 2000; Sankrit & Blair 2002). However, relatively low shock speeds and incipient radiative cooling made the interpretation of these shocks ambiguous (Long et al. 1992; Hester et al. 1994). Recently, Ghavamian et al. (2001) studied a filament on the northern boundary. It was chosen because there was no indication of the onset of radiative cooling. Indeed, the cooling time for the shock parameters derived below exceeds  $10^5$  years, while the flow time through the region of interest is 500 years. In addition, its morphology suggested a higher shock speed, making it easier to resolve the  $H\alpha$  profile.

Recent studies of SNR shocks have shown electron temperatures far below proton temperatures,  $T_e \ll T_p$ , in shocks faster than  $1000 \text{ km s}^{-1}$  (Raymond, Blair & Long 1995; Laming et al. 1996; Ghavamian et al. 2001) and ion temperatures approximately mass proportional to the proton temperatures,  $T_i \simeq (m_i/m_p)T_p$  (Raymond, Blair & Long 1995). This suggests that the plasma bulk velocity is randomized without efficient sharing of thermal energy among different particle species. Slower shocks, in particular the Cygnus Loop shock observed here, are much closer to electron-ion thermal equilibration. Ghavamian et al. (2001) derived a shock speed  $V_S$  of  $270$  to  $350 \text{ km s}^{-1}$  and  $T_e/T_i = 0.70$ - $1.0$  from the  $H\alpha$  line profile, the  $H\alpha$  to  $H\beta$  line ratio and the intensity ratio of broad to narrow components. Temperatures derived from X-ray observations in this region (De-courchelle et al. 1997) favor the upper ends of the allowed ranges,  $350 \text{ km s}^{-1}$  and  $T_e/T_i = 1.0$ . One might expect the kinetic temperatures of oxygen and hydrogen to be close to equilibrium as well.

A second aspect of the nature of SNR filaments is the 3-dimensional structure of the SNR shock. This is important for understanding the nature of the interaction between SNR blastwaves and density inhomogeneities. It is also needed to disentangle the pre-shock density,  $n_0$ , from the depth along the line of sight,  $L$ , for estimates of global SNR parameters. Hester (1987) demonstrated that SNR filaments are tangencies between the line-of-sight and a rippled sheet of optically thin emitting gas. The implied relationship between surface brightness and Doppler velocity

for the diffuse emission between the tangencies can be exploited to derive a 3D model of the shock (e.g., Raymond et al. 1988; Danforth et al. 2000). An alternative approach is to compare observables that depend on the line-of-sight depth,  $L$ , and the pre-shock density,  $n_0$ , in different ways. Szentgyorgyi et al. (2000) separated  $n_0$  and  $L$  in the XA region of the Cygnus Loop by comparing the intensity of a [Ne V] line, which scales as  $n_0 L$ , with the X-ray surface brightness, which scales as  $n_0^2 L$ . Patnaude et al. (2002) applied a similar technique to a recently shocked cloud in the SW Cygnus Loop.

A quantitative study of the O VI emission requires consideration of the effects of resonance scattering, both within the emitting sheet of gas and in the intervening ISM. The intrinsic intensity ratio of the resonance doublet of a Li-like ion is 2:1, but the 2:1 ratio of opacities implies a larger optical depth for the shorter wavelength line. Thus departures from a 2:1 ratio signal non-negligible optical depths in the O VI lines (Long et al. 1992; Sankrit & Blair 2002). Corbett et al. (1992) compared the optically thin emission in [O III]  $\lambda 5007$  with UV emission dominated by the C IV  $\lambda 1550$  doublet to show that bright filaments in the eastern Cygnus Loop are optically thick in the C IV lines. They confirmed that the filaments are tangencies to the line of sight and that resonance scattering is important for strong UV lines.

This paper presents O VI line profiles obtained with the FUSE satellite at 4 positions behind the filament investigated by Ghavamian et al. (2001) along with a low resolution FUV spectrum from the Hopkins Ultraviolet Telescope (HUT). The line widths are used to determine the degree of ion-ion thermal equilibration. The spectra yield both the line profile information and the intensity ratio information to permit both of the approaches described above to constraining the 3D structure of the shock. We construct models of the emission and scattering in the sheet of shocked gas to interpret the spectra. We find nearly complete equilibration between O and H, a pre-shock density about twice the value usually quoted for the Cygnus Loop blastwave, and a depth along the line of sight of about 0.7-1.5 pc. We also analyze the ROSAT PSPC X-ray image of the region. A thin, soft rim appears behind the filament in ROSAT data. We construct time-dependent ionization models to resolve the ambiguity between lower shock speed and emission from lower ionization states as causes of

the soft rim. We find that the soft rim at this location is largely due to strong emission from moderate ionization states in the region close to the shock.

## 2. Observations and Data Reduction

### 2.1. FUSE Observations

Spectra were obtained on 15 and 16 June, 2000 with the *Far Ultraviolet Spectroscopic Explorer* satellite (FUSE; Moos et al. 2000, Sahnow et al. 2000). A detailed discussion of the procedures and uncertainties related to FUSE observations of SNR filaments is given by Blair et al. (2002). Pointings were made at the four positions listed in Table 1 and shown in Figure 1. The uncertainty in the FUSE blind offset is believed to be about 1''. The image in Figure 1 is a superposition of H $\alpha$  (red) and [O III]  $\lambda 5007$  (green) images obtained through narrowband filters on the 1.2 m telescope at the Fred Lawrence Whipple Observatory on Mt. Hopkins on Nov. 7, 2000. Conditions were not photometric, and the seeing was about 1.6''. The image shows a portion of the H $\alpha$  filament complex that defines the northern edge of the Cygnus Loop. Faint H $\alpha$  emission well out in front of the main filaments reveals a portion of the blastwave in lower density gas. This is also apparent in the ROSAT image as faint X-ray emission ahead of the main edge of the remnant. A portion of the shock making the transition from non-radiative to radiative appears in [O III] emission at the southeast corner of the Figure 1. Very faint, diffuse [O II] and [O III] emission in the northeastern part of the image may arise from the partially ionized pre-shock gas (Bohigas et al. 1999).

As shown in the inset in Figure 1, the 20'' by 4'' MDRS aperture was placed parallel to the H $\alpha$  filament, at a position angle of 317° E of N. The aperture was placed on the brightest H $\alpha$  filament at the same position observed in the optical by Ghavamian et al. (2001). Subsequent slit positions were parallel to the first, but displaced 6.5'', 11'', and 15.5'' behind the first. The last position falls upon a fainter H $\alpha$  filament located about 15'' behind the bright one. Because of uncertain alignment between the LiF and SiC channels, we consider only the LiF data for the MDRS spectra.

Spectra through the 30'' by 30'' LWRS aperture were obtained simultaneously. The LWRS aperture

was located about  $3.5'$  to the northwest along the same filament complex, at the positions shown in Figure 1. The LWRS sensitivity is higher by the ratio of aperture areas. Moreover, the SiC channels can be used to extend the spectral coverage because the offset between LiF and SiC channels is relatively small compared to the LWRS aperture size. However, the LWRS significantly degrades the spectral resolution for extended emission. Especially when optical depth within the emitting gas or in the intervening ISM affects the line intensities, it is more difficult to derive reliable estimates of the intrinsic emission intensities. Therefore, the LWRS spectra are less useful for the purposes of this paper, and we discuss them only briefly below.

The data were processed with CalFUSE 2.0. We extracted MDRS spectra from the complete data set and also extracted spectra from the night portions of the orbits alone. The night-only extraction greatly reduced airglow, but it reduced the signal-to-noise of the O VI profiles so severely that we present only the data from the full exposures. For each MDRS pointing we shifted the Lif1a and Lif2B spectra to align the O I  $\lambda 1039.4$  airglow features, then added the Lif1a and Lif2b spectra weighted by the effective areas of those channels. The residuals around the fit to the dispersion solution for the LiF 2B segment are around  $5 \text{ km s}^{-1}$ . The Lif2B aperture may have drifted relative to the Lif1A aperture by a fraction of the slit width during the course of the observation, effectively broadening the aperture by 1 or  $2''$  (Blair et al. 2002). The absolute radiometric calibration of FUSE is believed to be good to 10%, and the relative calibration between  $1032 \text{ \AA}$  and  $1038 \text{ \AA}$  should be even better.

Figures 2a and 2b show the profiles of the O VI  $1032.93 \text{ \AA}$  and  $1037.61 \text{ \AA}$  lines at the four positions, with the uppermost profiles corresponding to the positions closest to the blastwave. Interstellar absorption in the C II  $\lambda 1037.02$  and H<sub>2</sub>  $\lambda\lambda 1037.15, 1038.16$  lines strongly affects the  $1037.61 \text{ \AA}$  line. While the interstellar lines lie at velocities of  $-171, -134$  and  $+158 \text{ km s}^{-1}$  with respect to the O VI line, we have no means to assess their effects except to compare the  $1032.93 \text{ \AA}$  and  $1037.61 \text{ \AA}$  line profiles. We assume that these absorption lines are important wherever the ratio  $I(1037)/I(1032)$  falls below its intrinsic value of 0.5. On that basis, interstellar absorption significantly attenuates the  $1037.61 \text{ \AA}$  emission at velocities

below about  $-60 \text{ km s}^{-1}$  and above about  $+90 \text{ km s}^{-1}$ .

Figure 3 shows the profile of O VI  $\lambda 1032$  from the sum of the LWRS exposures farther up the filament. The lower resolution of the LWRS smears the profile enough to mask the double peak structure if it is present. The asymmetry suggests that the diffuse region within the LWRS apertures is redshifted. The profile is similar to what one would expect from adding the profiles in Figure 2a and degrading the resolution to that of the LWRS, though the situation is more complicated because the intensity distribution across the LWRS aperture also affects the profile. One novel feature is present, however. The faint wing at redshifts above  $200 \text{ km s}^{-1}$  probably represents an additional component along the line of sight. Presumably this is due to the shock front associated with the faint H $\alpha$  and X-ray emission ahead of the filament observed by FUSE. If its speed is  $350 \text{ km s}^{-1}$  like that of the filament observed by FUSE, the shock must be viewed at about  $35^\circ$  to give the observed Doppler shift.

Table 2 presents the fluxes of the O VI lines at the four positions. It should be kept in mind that the 1037 line is attenuated by H<sub>2</sub> and C II interstellar lines, and that the effect of this absorption depends on the intrinsic line profile. The dereddened fluxes are based on  $E(B-V) = 0.08$  (Miller 1972) and the extinction curve of Cardelli, Clayton & Mathis (1989). H $\alpha$  fluxes computed by scaling the H $\alpha$  brightness in each MDRS aperture in the image in Figure 1 to surface brightness of a long slit spectrum of Ghavamian et al. (2001) are given for comparison. This scaling should lead to fluxes accurate to about 20%.

For completeness, Table 2 includes the O VI and C III  $\lambda 977$  fluxes measured from the sum of the 4 LWRS spectra. Because of the higher sensitivity of the LWRS spectra and the summation of 4 spectra, we avoid airglow contamination by using only data obtained during orbital night. The C III  $\lambda 977$  line is detected, but variations in the background subtraction limit the accuracy of the measured flux to  $\pm 40\%$ . Upper limits for other lines, such as Ne V]  $1136.5$  and Ne VI]  $1005.7$  are 2% the intensity of O VI  $\lambda 1032$ . Upper limits on the S VI  $\lambda\lambda 933.4, 944.5$  lines are about 6% of O VI  $\lambda 1032$  because of the lower sensitivity at the shorter wavelengths. The C III line is badly affected by interstellar absorption, so it is difficult to interpret. If resonant scattering attenuates the O VI intensity by a factor of 2 (see section 3.3.3), the strin-

gent limits on Ne V] and Ne VI] as compared to radiative shock models (Hartigan, Raymond & Hartmann 1987) confirm that this is a non-radiative shock.

## 2.2. HUT Observations

The Hopkins Ultraviolet Telescope (HUT; Davidsen et al. 1992) observed the non-radiative shock during the Astro-2 mission during March 1995. The 10'' by 56'' slit was centered at the position of the first FUSE observation with a position angle of 315°. The HUT aperture encompasses FUSE positions 1 and 2, and it extends nearly 3 times as far along the filament. Essentially all of the time when the Cygnus Loop was observable fell during orbital day, so the geocoronal background was high.

The HUT spectra cover the 912-1800 Å range with 3-4 Å resolution, and the radiometric calibration is accurate to about 10% (Kruk et al. 1999). Only the lines of He II, C IV and O VI were detected. The 2-photon continuum of hydrogen, C III  $\lambda$ 977 and the N V doublet at 1238, 1242 Å are expected to be strong in non-radiative shocks, but we could not reliably separate these features from the wings of geocoronal Ly $\alpha$  or Ly $\gamma$ .

Figure 4 shows the wavelength range that covers the C IV and He II lines as extracted from exposures totaling 2861 seconds. The O VI 1032 and 1037 lines are badly compromised by geocoronal emission at this resolution. Therefore, we report only the intensities of C IV  $\lambda\lambda$ 1548, 1550 and He II  $\lambda$ 1640. Comparison of measurements from the first and second pointings (1311 and 1550 seconds, respectively) indicates that fluctuations in the background level and the uncertainty in the double Gaussian fit dominate the uncertainties. We find intensities  $3.20 \pm 0.6$  and  $4.38 \pm 0.8 \times 10^{-13}$  erg cm $^{-2}$  s $^{-1}$ , respectively.

The lack of intercombination lines such as N IV]  $\lambda$ 1786 and O IV]  $\lambda$ 1400 confirms the non-radiative nature of the shock. In the models of radiative shocks these lines are comparable to C IV and He II in brightness (Hartigan, Raymond & Hartmann 1987). The lack of O IV] provides the stronger constraint, demonstrating that the shocked gas has not yet cooled to  $2 \times 10^5$  K.

## 2.3. ROSAT Observations

ROSAT PSPC observations of the Cygnus Loop have been presented by Levenson et al. (1999). The filament observed here is about 20' east the center of their 3506 second North (E) region exposure. For the purposes of this paper, we extracted PSPC spectra of fourteen 25'' by 250'' bands parallel to the filament for comparison with theoretical shock models. The 25'' width is comparable to the spatial resolution of the PSPC, so the spectra are not entirely independent. Single temperature fits with a Raymond & Smith (1977) ionization equilibrium model yield temperatures increasing from 0.14 to 0.2 keV over a distance of about 1' behind the shock. However, ionization equilibrium is a poor approximation close to the shock. We therefore fold the spectra predicted by the shock models through the ROSAT effective area to compute the PSPC count rate as a function of position behind the shock. The models and results are discussed in section 3.3.4.

## 3. Analysis

### 3.1. Resonance Scattering

Before attempting to interpret the line profiles, we need an estimate of the optical depths in the O VI lines. Models based on the code described by Raymond (1979) and Cox & Raymond (1985) predict optical depths of 0.01 to 0.1 along the flow direction. The filament observed by FUSE is viewed nearly edge-on, so the optical depths are much larger. Because the emitting sheet of gas is much thicker along the line of sight than in the flow direction, the main effect of finite optical depth is to scatter photons out of the line of sight. As the optical depth in the  $\lambda$ 1032 line is twice as large as that in  $\lambda$ 1037, the intensity of  $\lambda$ 1032 is more strongly affected, and the intensity ratio  $I(1032)/I(1037)$  drops below its intrinsic value of 2:1

For a slab geometry and the approximation of single scattering, the intensity of a line is given by

$$I = \epsilon (1 - e^{-\tau}) \quad (1)$$

where  $\epsilon$  is the ratio of emissivity to opacity. The factor  $\epsilon$  includes the collision strength, the oscillator

strength, the electron density and factors involving the electron temperature and the O VI line width. All these factors are nearly constant in the ionization zone just behind a non-radiative shock, so  $\epsilon$  is nearly constant. In that case, the effects of resonance scattering can be assessed from the ratio

$$R \equiv \frac{2 I(1037) - I(1032)}{2 I(1037)} = \frac{2(1 - e^{-\tau_{1037}}) - (1 - e^{-\tau_{1032}})}{2(1 - e^{-\tau_{1037}})} \quad (2)$$

with  $\tau_{1032} = 2\tau_{1037}$ . The ratio varies from 0 for  $\tau=0$  to 0.5 for  $\tau=\infty$ .

Figure 5 shows the observed ratios R for Positions 1 and 4, and Figure 6 shows the function given in Equation 2. The ratios for Positions 2 and 3 are roughly 0.1, but they are quite noisy. The solid parts of the curves are the velocity ranges where the data are reliable. The dotted portions are regions where C II or H<sub>2</sub> interstellar absorption affects the profile, or where the signal in the 1037 line is too low to give a reliable ratio.

Figures 5 and 6 imply optical depths  $\tau_{1037}$  of order 1-3 through the emitting regions of Positions 1 and 4. At Positions 2 and 3 the ratios are smaller, suggesting optical depths of 0.3 to 0.5. The smaller optical depths are consistent with the morphological indication that the line of sight is farther from tangency at positions 2 and 3. In a small portion of the range in Figure 5a near a velocity of 0 km s<sup>-1</sup> R exceeds the theoretical maximum of 0.5. This is presumably due to interstellar absorption, which scatters  $\lambda 1032$  photons more effectively than  $\lambda 1037$  photons, but does not compensate by emitting correspondingly more  $\lambda 1032$  photons. However, Figure 5b does not show a corresponding peak at position 4. This suggests that a combination of intrinsic and interstellar scattering is required to account for the peak in Figure 5a.

### 3.2. Thermal Equilibration

The discussion above shows that optical depth can affect the line profiles, but the rough constancy of R in Figure 5 suggests that scattering affects the overall intensity more than it distorts the line profile. Comparison of the O VI profiles obtained from the the

LiF 1A and LiF 2B channels indicates that the fluctuations in Figure 5 are marginally real. The most stringent limit on the line width comes from the sharp feature at  $V = +25$  km s<sup>-1</sup> in the profile for Position 4 that arises from the trailing filament seen in Figure 1. Based on Figures 5b and 6, the optical depth at the peak of the bright feature in the  $\lambda 1032$  profile at Position 4 is about 1.5, and the flux is attenuated by about a factor  $(1 - e^{-\tau})/\tau$ , or about 0.52. The fluxes at the apparent half-power points at -20 km s<sup>-1</sup> and +60 km s<sup>-1</sup>, on the other hand, are attenuated by factors of 0.63 and 1.0, respectively. Therefore, the line profile has been broadened by attenuation at its peak, and the apparent Full Width Half Maximum of 120 km s<sup>-1</sup> corresponds to a 90 km s<sup>-1</sup> intrinsic width. It is clear from the profiles of Positions 1 to 3 and from the blue wing of the Position 4 profile that bulk motions also contribute to the Doppler width. There is no reliable way to assess the bulk velocity contribution, however, so we use the observed line width corrected for resonance scattering as an upper limit to the oxygen kinetic temperature

$$T_O < 2.7 \times 10^6 \text{ K} \quad (3)$$

This can be compared with the proton temperature of  $T_p = 1.4 \pm 0.35 \times 10^6$  K derived from the H $\alpha$  line width by Ghavamian et al. (2001). The time scale for O<sup>5+</sup> ions to slow by Coulomb collisions corresponds to a distance of  $\sim 10\text{-}15''$  behind the shock for the density range derived below (Spitzer 1968), while the O VI emissivity peaks only 1'' behind the shock in the model presented below. Therefore, the upper limit in  $T_O$  applies to the immediate post-shock region. Thus the upper limit to the ratio of oxygen to hydrogen kinetic temperatures is 2.5 including the uncertainty in the proton temperature.

For comparison, Raymond et al. (2000) and Mansuso et al. (2002) found O VI line widths near 3/4  $V_s$  (FWHM) for 1000 km s<sup>-1</sup> shocks in the solar corona. The 350 km s<sup>-1</sup> Cygnus Loop shock shows a line width below 1/4  $V_s$ . The Alfvén Mach number, defined as the shock speed divided by the Alfvén speed, might be a parameter that controls heating in the shock. In spite of their high speeds, the shocks in the solar corona had modest Alfvén Mach numbers and modest compressions. The Cygnus Loop shock has a lower speed, but probably a higher Alfvén Mach number. Berdichevsky et al. (1997) found He and O kinetic temperatures roughly twice the

mass ratios times the proton temperatures in shocks in the solar wind. Few observations of ion temperatures in supernova remnant shocks are available. Roughly mass-proportional temperatures,  $T_C \sim 12T_p$  and  $T_{He} \sim 4T_p$ , were found in a  $2300 \text{ km s}^{-1}$  shock in SN1006 (Raymond, Blair & Long 1995).

We find that for this  $350 \text{ km s}^{-1}$  shock  $T_O \sim T_p \sim T_e$  even though its Alfvén Mach number is fairly high, as opposed to faster shocks in which  $T_O > T_p > T_e$ . On the other hand, fast shocks in the solar wind with modest Alfvén Mach numbers also show  $T_O > T_p > T_e$ . This suggests that shock speed rather than Alfvén Mach number may control the thermal equilibration.

### 3.3. Structure in 3 Dimensions

It is not practical to invert the observed  $H\alpha$  image and the O VI profiles to obtain the shape of the shock, because the effects of resonance scattering are complicated and sensitive to both the viewing angle and the geometrical structure (e.g., Wood & Raymond 2000). Therefore, we proceed by constructing a model, computing the line intensities and profiles for the 4 positions, and adjusting the model parameters to optimize the fit. We first discuss the overall nature of the structure and its relationship to the measured profiles, then describe the model, and finally present the results.

#### 3.3.1. Model Framework

The  $H\alpha$  filaments clearly represent the projection of a rippled sheet on to the plane of the sky as proposed by Hester (1987). The surface brightness of the shock seen face-on is the product of the number of H atoms swept up per second and the number of photons emitted by an H atom before it is ionized, which is given by the ratio of excitation and ionization rates.

$$I_0 = \frac{1}{4\pi} n_{H0} V_s \frac{q_{ex}}{q_{ion}} \text{ photons cm}^{-2} \text{ s}^{-1} \text{ sr}^{-1} \quad (4)$$

For the nearly edge-on viewing angle of the filaments, the brightness is increased by a factor  $\sec(\theta)$ , where  $\theta$  is the angle between the line-of-sight and the shock normal. As  $\theta$  approaches  $90^\circ$ , the geometrical enhancement is limited to  $L/l_{\text{obs}}$ , where  $L$  is the depth

along the line-of-sight and  $l_{\text{obs}}$  is the larger of the thickness of the emitting layer and the spatial resolution element. The two nearly parallel bright filaments covered by the FUSE MDRS slit positions are tangencies between the line-of-sight and the emitting sheet, and the diffuse region in between is where the sheet curves away from tangency.

An equation similar to Equation 4 describes the O VI intrinsic brightness, but with  $n_O$  replacing  $n_{H0}$  and the excitation and ionization rates for the O VI lines replacing those of  $H\alpha$ . However, the projection of the O VI brightness is more complicated. The thickness of the  $H\alpha$  emitting sheet is smaller than the resolution of the images,  $< 10^{15} \text{ cm}$  in the models presented here, and the  $H\alpha$  line is optically thin. For the O VI lines, on the other hand, the emitting sheet is roughly  $5''$  thick. The optical depths discussed above present an even greater complication. The line profiles are determined by the emissivity as a function of position, the line-of-sight component of the bulk velocity of the shocked gas, the thermal velocity profile of the O VI ions, and the optical depth as a function of position and velocity. We adopt an oxygen abundance of 8.73 from Holweger (2001). This is lower than the widely used value of 8.82, but it is supported by the work of Allende Prieto, Lambert & Asplund (2001). The emitting layer is thin enough that radiative cooling has no effect, so the abundances of other elements do not affect the predictions for O VI.

#### 3.3.2. O VI Profile Models

The emissivity and opacity behind a planar shock wave are computed by the code described in Raymond (1979) and Cox & Raymond (1985), which has been updated to allow electron and ion temperatures to evolve separately. The model parameters are shock speed, pre-shock density, pre-shock ionization state, pre-shock magnetic field, and the ratio of electron to ion temperature at the shock. The magnetic field and pre-shock ionization state have little effect on the O VI emission and absorption, and they are fixed at a neutral hydrogen fraction of 0.5 and a field of  $3 \mu\text{G}$ . The electron-proton temperature equilibration was investigated by Ghavamian et al. (2001), and in the  $T_e/T_p > 0.7$  range they found, the initial electron-ion temperature ratio also has little effect. In the extreme non-equilibrium case  $T_e/T_p = 0.05$ , the thickness of the O VI emitting layer is roughly

twice as large as it is for the  $T_e/T_p = 1$  models we adopt.

The model code starts with the Rankine-Hugoniot jump conditions, then computes the density, velocity,  $T_e$  and  $T_i$ , and the time-dependent ionization state of the shocked gas. Because we are interested only in the narrow ionization zone behind the shock, the density is very close to 4 times the pre-shock density, and the velocity in the shock frame is very close to 1/4 the shock speed throughout. For nearly complete electron-ion equilibration in the shock, the temperature is also nearly constant in the emitting region. Thus the only important parameters are  $V_s$  and  $n_0$ . The O VI excitation and ionization rates are fairly weak functions of temperature above  $10^6$  K, and the O VI thermal line width scales as  $T_O^{1/2}$ . The thickness of the shock structure scales as  $n_0^{-1}$ , the opacity scales as  $n_0$  and the local emissivity as  $n_0^2$ .

The shape of the shock front along the line of sight is parameterized as

$$Y = aX + b \sin(\pi X/c) \quad (5)$$

where  $X$  is the distance along the line of sight and  $Y$  is distance in the plane of the sky. While this form imposes a symmetry on the structure, the data do not warrant a function having more parameters. The models used a pixel size of  $6.6 \times 10^{15}$  cm, or  $1.0''$  at 440 pc. We also assume that the shock speed and preshock density are constant along the shock front. Allowing them to vary would introduce unresolvable ambiguities. We use the density, temperature and O VI concentration from the planar shock models to compute the opacity and emissivity in the O VI lines at positions behind the shock. The opacity and emissivity are computed at  $10 \text{ km s}^{-1}$  resolution using the O VI line width, shifted by the line-of-sight component of the bulk speed. We adopt an oscillator strength  $f_{1032} = 0.13$  (Morton 1991), an excitation rate coefficient  $q_{1032} = 1.5 \times 10^{-8} \text{ cm}^3 \text{ s}^{-1}$  (Zhang, Sampson & Fontes 1990), and an ionization rate from Younger (1981).

The interstellar O VI absorption is an “external” parameter of the models. Shelton & Cox (1994) found that the galactic O VI column includes a Local Bubble component of  $N_{\text{OVI}} = 1.6 \times 10^{13} \text{ cm}^{-2}$  and absorbing regions of  $N_{\text{OVI}} = 2 - 7 \times 10^{13} \text{ cm}^{-2}$  separated by 400-1300 pc. The Cygnus Loop emission will be absorbed by the Local Bubble component and perhaps by one other absorbing region. The ISM absorption

is taken to have a temperature of  $10^6$  K. The widths of individual O VI absorption components may correspond to  $3 \times 10^5$ , but multiple components along the line of sight can result in typical line widths corresponding to  $10^6$  K (Jenkins & Meloy 1974). The Local Bubble alone produces a dip of about 15% at zero velocity. The central peak in Figure 5a suggests some interstellar absorption in that it rises above 0.5. It is consistent with a total column  $N_{\text{OVI}} = 7 \times 10^{13} \text{ cm}^{-2}$ .

The model code computes the surface brightness

$$I(Y, V) = \frac{1}{4\pi} \int \epsilon(X, Y, V) e^{-\tau(X, Y, V)} dX \text{ photons cm}^{-2} \text{ s}^{-1} \text{ sr}^{-1} \quad (6)$$

for the  $\lambda 1032$  and  $\lambda 1037$  lines, and we average the profiles over  $4''$  in  $Y$  to compare with the FUSE observations. Figure 8 shows model predictions for the  $\lambda 1032$  profiles at the 4 slit positions in the same format as the observed profiles in Figure 2. As in Table 2, we assume a factor of 2.8 attenuation due to reddening. This model assumes  $V_s = 350 \text{ km s}^{-1}$ , a pre-shock density of  $0.5 \text{ cm}^{-3}$  and an interstellar column density  $N_{\text{OVI}} = 0.7 \times 10^{14} \text{ cm}^{-2}$ . The shape parameters of the emitting sheet were  $a = -0.17$ ,  $b = 28$  and  $c = 300$ . The shape is shown in Figure 7, but note the order of magnitude difference in the  $X$  and  $Y$  scales. This model assumed an oxygen kinetic temperature equal to the proton temperature in the O VI emitting region. Figure 9 shows the predictions for the intensity ratio  $R$  shown in Figure 5.

To examine the effect of changes in the pre-shock density, we computed the O VI  $\lambda 1032$  profiles for a model with  $n_0 = 0.3 \text{ cm}^{-3}$ . The total number of photons emitted scales directly as  $n_0$ , and the profiles in Figure 9 are very close to those in Figure 7a scaled by a factor of  $3/5$ . The optical depths in both models are similar, because the density in the  $n_0 = 0.3 \text{ cm}^{-3}$  is smaller, but the thickness of the O VI layer is larger by the same factor because the cooling length increases. There are departures of order 10% from the  $3/5$  scaling because the areas extracted for FUSE positions 1 through 4 correspond to slightly different parts of the post-shock ionization structure.

To illustrate the effects of optical depth, Figure 10 shows the intrinsic profile emitted at position 1 and the profile after the effects of resonant scattering and interstellar absorption. The observed profile is attenuated by a further factor of 2.8 by reddening. The dip at line center is largely due to interstellar absorption.

The profile without ISM absorption would be nearly flat between the two peaks. The net effect of scattering, which is dominated by scattering within the emitting sheet, is to reduce the O VI flux by about a factor of 2.

The resonance scattering will also affect the C IV intensity measured by HUT. However, the effect may be less severe than for the FUSE observations, because the HUT aperture is larger and more of it is filled by diffuse emission that arises from more face-on portions of the shock. The relative intensities of the C IV and He II lines are in reasonable agreement with the predictions of models such as that described in section 3.3.1 for a  $350 \text{ km s}^{-1}$  shock provided that carbon is depleted by a factor of 2-3 and that resonance scattering (perhaps dominated by the interstellar C IV absorption) further attenuates the C IV flux by a factor of 2-3.

As a check on the model parameters we compare the H $\alpha$  fluxes at 4 FUSE positions with the figures in Table 2. Each neutral hydrogen atom passing through the shock emits 0.25 H $\alpha$  photons on average, and the shock emits

$$I_0(H\alpha) = 0.25 n_{H^0} V_s / 4\pi \text{ photons/cm}^2 \text{ s sr} \quad (7)$$

and the area within each FUSE position can be computed from Equation 5. The computed H $\alpha$  fluxes are 0.019, 0.017, 0.022 and 0.025 photons  $\text{cm}^{-2} \text{ s}^{-1}$  for 4" by 20" boxes at the four positions respectively for  $n_{H^0} = 1.0$ . The fluxes at the first and last positions are extremely sensitive to the exact position, changing by nearly a factor of 2 with shifts of 1" in the position. The variation with position roughly matches that in Table 2, but with significant scatter. The ratio of the total of the predicted fluxes to the total of the observed H $\alpha$  fluxes is 4.0  $n_{H^0}$ . Thus the predictions match observations for  $n_0=0.5$  and a pre-shock neutral fraction of 0.5. Calculation of the flux of ionizing photons from such a shock, mainly He $^0 \lambda 584$  and He $^+ \lambda 304$ , suggests an upper limit on the pre-shock neutral fraction of 0.7 (e.g., Smith et al. 1994; Ghavamian et al. 2000). Comparison of the O VI and H $\alpha$  fluxes in Table 2 with the model prediction  $I_{1032}/I_{H\alpha} \sim 12$  (and considering the factor of 2 attenuation of  $I_{1032}$  derived above) suggests a neutral fraction near 1. On the other hand, Ghavamian (1999) used the ratio of the He II  $\lambda 4686$  line to H $\beta$  in this filament to derive an upper limit of 0.2 for the pre-shock neutral fraction. This would require

a preshock density  $n_0 > 1.25$ . Such a high density would imply an extremely small depth along the line of sight to match the ROSAT X-ray brightness (see section 3.3.4), of order 0.1 pc. This small depth would increase the curvature of the sheet by a factor of 7, resulting in a very large separation of the peaks in the O VI profile. Thus we prefer the parameters  $n_0 \sim 0.5$  and a high neutral fraction.

### 3.3.3. Comparison to Observed O VI Profiles

Figure 8 shows overall qualitative agreement with the intensity and a line shape that evolves from double peaked near the primary shock toward single peaked where the emission from the trailing tangency dominates. As in the observed spectra, the flux is highest at position 1, declines through positions 2 and 3, then increases again at position 4.

In detail, there are two discrepancies. First, the separation of the peaks at position 1 is predicted to be only about  $85 \text{ km s}^{-1}$ , while the observed separation is  $110 \text{ km s}^{-1}$ . The predicted separations increase to 95 and  $105 \text{ km s}^{-1}$  at positions 2 and 3, closer to the observed separations, but still somewhat smaller. Second, while the predicted red peak at position 4 is closer to zero velocity than at position 3, as observed, the predicted blue peak is nearly as strong as the red peak, while the observed blue peak is much fainter. The faint blue peak probably results from lower pre-shock density in the region producing that part of the profile. The separations of the peaks at positions 1-3 present a more substantial problem.

The separations of the peaks are partly due to the interstellar absorption and partly to the line-of-sight velocity components of the shocked gas. The ISM absorption cannot plausibly be made much broader, but a higher shock speed or a larger curvature, yielding larger angles between the line of sight and the shock front, would increase the separation. A higher curvature would require a compensating density increase to maintain the surface brightness, and  $n_0 = 0.5$  is already rather high in comparison with X-ray observations discussed below. A higher shock speed would be difficult to reconcile with the H $\alpha$  line width measured by Ghavamian et al. (2001).

The predicted separations of the peaks could also be increased by relaxing some of the assumptions inherent to the model. We have assumed the flow to be perpendicular to the shock surface, as will occur for

a shock driven by gas pressure. An oblique magnetic field can introduce a velocity component along the shock surface, but for the parameters considered here and fields below  $10 \mu\text{G}$ , this will less than about  $1 \text{ km s}^{-1}$  according to the shock jump conditions (McKee & Hollenbach 1980). It is also possible to maintain oblique shocks if the ram pressure of the flow is significant, for instance as occurs in bow shocks. The steepest angle in the model sheet is  $6^\circ$ , so the parallel component of the post-shock flow speed should be small, but flows along the shock at  $\sim 20 \text{ km s}^{-1}$  in the sense expected for oblique shocks could account for the observed peak separations.

Another explanation would involve cosmic ray acceleration. We have assumed the the post-shock flow speed of a gasdynamic shock,  $3/4 V_S$ . If a significant fraction of the energy dissipated in the shock goes into accelerating cosmic rays, the shock compression is larger than 4, and the post-shock flow speed is larger than  $3/4 V_S$ . This explanation would require higher shock speeds to match observed  $\text{H}\alpha$  profile and X-ray temperature. If most of the energy dissipated goes into cosmic rays, a shock several times faster may be needed (Boulares & Cox 1988). The higher shock speeds would imply a greater distance to the Cygnus Loop in order to match measured filament proper motions. The O VI and  $\text{H}\alpha$  surface brightnesses are proportional to the number of particles swept up per second, so the higher shock speed would imply a smaller density.

### 3.3.4. ROSAT Data

It is important to check the consistency of the derived parameters against the ROSAT X-ray images of the Cygnus Loop. Levenson et al. (1999) included the region we observe in their study of the narrow soft rim in PSPC images. Miyata & Tsunemi (1999) observed an area just to the East in a study of elemental abundances and they favored idea that the blastwave has recently reached the wall of a cavity. Decourchelle et al. (1997) studied the region just to the West, exploring the multiple temperature components needed to explain the brighter, softer emission regions.

Figure 11 shows the ROSAT counts extracted in  $25''$  by  $250''$  bins parallel to the filament. The position of the main  $\text{H}\alpha$  filament is taken as zero, and 440 pc is taken as the distance to the Cygnus Loop

(Blair et al. 1999). Models were computed with the Raymond (1979) code and Allen (1973) abundances. The curves show model predictions for a  $350 \text{ km s}^{-1}$  shock with preshock densities of  $0.2$  and  $0.3 \text{ cm}^{-3}$ . The X-ray emissivities predicted by the shock model are attenuated by an interstellar column  $N_H = 1.5 \times 10^{20} \text{ cm}^{-2}$  and multiplied by the ROSAT PSPC effective area and exposure time. A somewhat higher  $N_H$  is often assumed for the Cygnus Loop, but Decourchelle et al. (1997) require  $N_H \simeq 1 \times 10^{20} \text{ cm}^{-2}$  to match the very soft X-ray spectra just to the west of the position we observed. The model predictions have been added to an assumed background Cygnus Loop emission of 1500 counts estimated from the brightness ahead of the filament. The predicted X-ray counts were scaled to line-of-sight depths of 2 and 4 pc, respectively, for  $n_0 = 0.3$  and  $0.2 \text{ cm}^{-3}$ . The higher pre-shock density  $n_0 = 0.5$  used for the O VI profile models would produce a curve higher and narrower than the solid curve in Figure 11, but the spatial resolution of the PSPC would smear it to agree reasonably well with the measured values if the line of sight depth is scaled to about 0.7 pc. The PSPC resolution would smear the  $0.2 \text{ cm}^{-3}$  predictions to be broader than the observed points, so we conclude that  $n_0 > 0.2 \text{ cm}^{-3}$ .

The post-shock density and temperature are essentially constant, and the peak in the predicted brightness results from the presence of moderate ionization stages that emit efficiently in the soft (0.25 keV) part of the ROSAT bandpass before the gas reaches ionization equilibrium. This departure from ionization equilibrium also produces a lower temperature in simple fits to the ROSAT spectrum, accounting for the gradual rise from  $kT = 0.14 \text{ keV}$  to  $kT = 0.2 \text{ keV}$  over a distance of about  $5 \times 10^{17} \text{ cm}$  in the fitted temperatures.

The models are planar, so any bending of the surface will broaden the profile compared with the model profiles. The  $0.3\text{--}0.5 \text{ cm}^{-3}$  models require a path length comparable to that suggested by the O VI observations, while a preshock density of  $0.2$  requires twice that value. A lower interstellar column,  $N_H = 10^{20} \text{ cm}^{-2}$  would bring the  $n_0 = 0.2$  model into agreement with the O VI model and push the higher density model to a shorter length scale. We conclude that  $n_0 = 0.3\text{--}0.5 \text{ cm}^{-3}$  and  $L=0.7\text{--}1.5 \text{ pc}$  are consistent with both the FUSE and ROSAT data. We note, however, that the soft X-ray rim predicted by the model arises mostly from C, Si and Fe emis-

sion lines, and that these elements may be locked up in grains, as suggested by the C IV flux measured by HUT. If they are liberated by sputtering over a swept-up column of order  $10^{18} \text{ cm}^{-2}$  (Vancura et al. 1994), the peak will be suppressed.

The soft rim seen in the ROSAT hardness ratio map of the Cygnus Loop was used by Levenson et al. (1999) to support the idea that the Cygnus Loop blastwave recently encountered the shell of a cavity created by the progenitor star. As Levenson et al. (1999) point out, the soft emission in the X-ray bright regions can result from a slower shock speed in denser material. They note that in the non-radiative regions such as the one examined here, the rim could result either from a higher density when the shock encounters the shell, or from the non-equilibrium ionization effect illustrated in Figure 11. We find that non-equilibrium ionization can account for the soft rim in this region, but only if the refractory elements are present in the gas phase without serious depletion. We favor a preshock density somewhat higher than the canonical value of  $0.2 \text{ cm}^{-3}$ . This may be related to the lag between the outer faint emission seen in Figure 1 and the filament we observed. Thus while the soft rim is solid evidence for recent interaction with dense gas in the regions bright in X-rays and optical emission, its interpretation is still ambiguous in the Balmer-dominated filaments in the northern Cygnus Loop.

#### 4. Summary

Far UV observations of the O VI lines in a non-radiative shock in the northern Cygnus Loop show that the oxygen and proton temperatures are fairly close to equilibrium;  $T_O/T_p < 2.5$ . This is consistent with the effective electron-ion equilibration in this shock inferred by Ghavamian et al. (2001) and effective ion-ion equilibration, as opposed to the strong preferential heating of oxygen measured in faster shocks in the solar wind.

The O VI line profiles show clear evidence for resonance scattering, both in the profile shapes and in the intensity ratio of the  $\lambda 1032$  and  $\lambda 1037$  lines. While there is some uncertainty as to the relative contributions of interstellar O VI opacity and opacity within the emitting sheet of gas, optical depths  $\tau_{1037} \simeq 0.5 - 2$  are required, with the highest optical

depths in the bright filaments and at small velocities. The opacity effects reduce the total line intensity of the  $1032$  line by roughly a factor of 2.

The line shapes and intensities make it possible to estimate the structure of the emitting sheet along the line of sight, and to infer a pre-shock density. These estimates can be checked against ROSAT data. We find a depth along the line of sight of 0.7 to 1.5 pc and a pre-shock density of  $0.3-0.5 \text{ cm}^{-3}$ . A shock speed of  $350 \text{ km s}^{-1}$  at the upper end of the range allowed by the  $H\alpha$  profile (Ghavamian et al. 2001) is needed to match the FUSE and ROSAT data. The above parameters support that conclusion to some extent, in that the pre-shock density is roughly twice the canonical value, but part of that difference results from the difference between the 440 pc distance to the Cygnus Loop and the 770 pc distance used in earlier analyses.

Levenson et al. (1999) used the soft outer edge of the Cygnus Loop in ROSAT images to conclude that the blast wave is slowing down due to a very recent encounter with higher density material. The shock model shows that departure from ionization equilibrium can contribute to the softness of the ROSAT spectrum in the outer  $1-2'$  behind the Balmer line filaments, reducing the need for a density enhancement in this region.

This work was made possible by the dedication of the teams that built and operate the FUSE satellite. It was performed under NASA Grant NAG5-9019 to the Smithsonian Astrophysical Observatory and G00-1035X and G01-2052X to Rutgers University.

## REFERENCES

Allen, C.W. 1973, *Astrophysical Quantities*, Third Edition, The Athlone Press, London, p. 31

Allende Prieto, C., Lambert, D.L., & Asplund, M. 2001, ApJ Lett, 556, L63

Berdichevsky, D., Geiss, J., Gloeckler, G., & Mall, U. 1997, JGR, 102, 2623

Blair, W.P., Sankrit, R., Raymond, J.C., & Long, K.S. 1999, AJ, 118, 942

Blair, W.P., Sankrit, R., & Tulin, S. 2002, APJS, 140, 367

Blair, W.P., et al. 1991, ApJ, 379, L33

Bohigas, J., Sauvageot, J.L., Decourchelle, A. 1999, A&A, 318, 324

Boulares, A., & Cox, D.P. 1988, ApJ, 333, 198

Cardelli, J.A., Clayton, G.C., & Mathis, J.S. 1989, ApJ, 345, 245

Chevalier, R.A., & Raymond, J.C. 1978, ApJ, 225, L27

Chevalier, R.A., Kirshner, R.P., & Raymond, J.C. 1980, ApJ 235, 186

Cornett, R.H., et al. 1992, ApJ, 395, 9

Cox, D.P., & Raymond, J.C. 1985, ApJ, 298, 651

Danforth, C.W., Cornett, R.H., Levenson, N.A., Blair, W.P., & Stecher, T.P. 2000, AJ, 119, 2319

Davidson, A.F., et al. 1992, ApJ, 392, 264

Decourchelle, A., Sauvageot, J.L., Ballet, J., & Aschenbach, B. 1997, A&A, 326, 811

Fesen, R.A., & Itoh, H. 1985, ApJ, 295, 43

Ghavamian, P. 1999, PhD Thesis, Rice University

Ghavamian, P., Raymond, J., Blair, W., & Hartigan, P. 2000, ApJ, 535, 266

Ghavamian, P., Raymond, J., Smith, R.C., & Hartigan, P. 2000, ApJ, 547, 995

Hartigan, P., Raymond, J., & Hartmann, L. 1987, ApJ, 316, 323

Hester, J.J. 1987 ApJ, 314, 187

Hester, J. J., Raymond, J.C., & Blair, W.P. 1994, ApJ, 420, 721

Holweger, H., in *Solar and Galactic Composition*, R.F. Wimmer-Schweingruber, ed., (Melville, NY: AIP), p. 23

Jenkins, E.B., & Meloy, D.A. 1974, ApJ, 193, L121

Kruk, J.W., Brown, T.B., Davidsen, A.F., Espey, B.R., Finley, D.S., & Kriss, G.A. 1999, ApJS, 122, 299

Ku, W.H.-M., Kahn, S.M., Pisarski, R., & Long, K.S. 1984, ApJ, 278, 615

Laming, J.M., Raymond, J.C., McLaughlin, B.M., & Blair, W.P. 1996, ApJ, 472, 267

Levenson, N.A., Graham, J. R., Keller, L. D., & Richter, M. 1998, ApJS, 118, 541

Levenson, N. A., Graham, J. R., & Snowden, S. L. 1999, ApJ, 526, 874

Long, K.S., Blair, W.P., Vancura, O., Bowers, C.W., Davidsen, A.F., & Raymond, J.C. 1992, ApJ, 400, 214

Mancuso, S., Raymond, J.C., Kohl, J., Ko, Y.-K., Uzzo, M., & Wu, R. 2002, A&A 383, 267

McKee, C.F., & Hollenbach, D. 1980, Ann. Revs. Astr. Ap., 18, 219

Miller, J.S. 1974 ApJ, 189, 239

Miyata, E., & Tsunemi, H. 1999, ApJ, 525, 305

Moos, H.W., et al. 2000, ApJ, 538, L1

Morton, D.C. 1991, ApJS, 77, 119

Patnaude, D.J., Fesen, R.A., Raymond, J., Levenson, N.A., Graham, J., & Wallace, D.J. 2002, submitted to ApJ

Raymond, J.C. 1979, ApJS, 39, 1

Raymond, J.C. 2001, SSRV, 99, 209

Raymond, J.C., & Smith, B.W. 1977, ApJS, 35, 419

Raymond, J.C., et al. 1980, ApJ, 238, L21

Raymond, J.C., Hester, J.J., Cox, D.P., Blair, W.P., Fesen, R.A., & Gull, T.R. 1988, ApJ, 324, 869

Raymond, J.C., Hester, J.J., Blair, W.P., Fesen, R.A., & Gull, T.R. 1988, ApJ, 324, 869

Raymond, J.C., Blair, W.P., & Long, K.S. 1995, ApJ, 454, L31

Raymond, J.C., Thompson, B.J., St.Cyr, O.C., Gopalswamy, N., Kahler, S., Kaiser, M., Lara, A., Ciaravella, A., Romoli, M., & O'Neal, R. 2000, GRL, 27, 1493

Sahnow, D.J., et al. 2000, ApJ, 538, L7

Sankrit, R., Blair, W.P., Raymond, J.C., & Long, K.S. 2000, AJ, 120, 1925

Sankrit, R., & Blair, W.P. 2002, ApJ, 565, 297

Shelton, R.L., & Cox, D.P. 1994, ApJ, 434, 599

Shull, P.J., Dyson, J.E., Kahn, F.D., & West, K. A 1985, MNRAS, 212, 799

Shull, P.J., & Hippelein, H. 1991, ApJ, 383, 714

Smith, R.C., Raymond, J.C., & Laming, J.M. 1994, ApJ, 420, 286

Spitzer, L. 1968, *Diffuse Matter in Space* (New York: Wiley), p. 94

Szentgyorgyi, A.H., Raymond, J.C., Hester, J.J., & Curiel, S. 2000, ApJ, 529, 279

Treffers, R.R. 1981, ApJ, 250, 213

Vancura, O., Blair, W.P., Long, K.S., Raymond, J.C., & Holberg, J.B. 1993, ApJ, 417, 663

Vancura, O., Raymond, J.C., Dwek, E., Blair, W.P., Long, K.S. & Foster, S. 1994, ApJ, 431, 188

Wood, K., & Raymond, J. 2000, ApJ, 540, 563

Younger, S.M. 1981, *J. Quant. Spectr. Rad. Transf.*, 26, 329

Zhang, H.L., Sampson, D.H., & Fontes, C.J. 1990, ADNDT, 44, 31

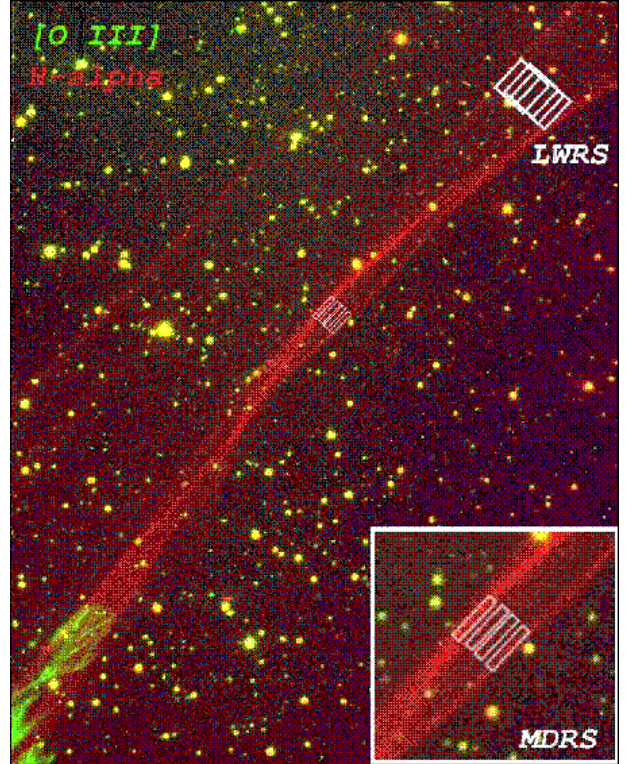


Figure 1: Images of the northern Cygnus Loop Balmer line filaments in H $\alpha$  (red) and [O III]  $\lambda 5007$  (green). North is at the top and East at the left. The image is 7.3' by 9.2'. An expanded view of the 4 MDRS slit positions is shown in the inset. The 4 overlapping LWRS exposures lie on the diffuse emission near the NW corner. Positions 1 through 4 progress from northeast to southwest. The 30'' size of the LWRS aperture shows the scale.

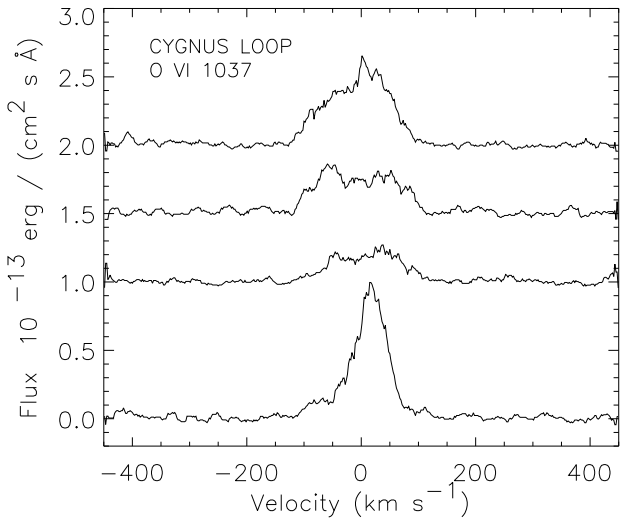
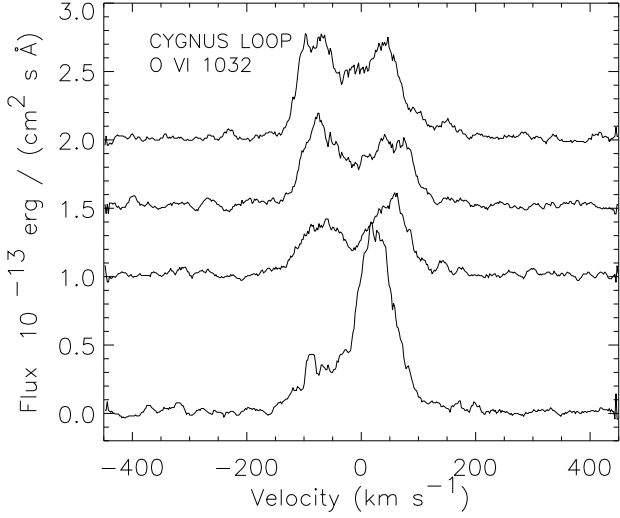


Figure 2 – (a) O VI  $\lambda 1032$  line profiles for the four MDRS slit positions, with the topmost profile corresponding to the leading filament. Profiles of Positions 1, 2 and 3 are offset by 2.0, 1.5 and 1.0 to avoid overlap. (b) Same for O VI  $\lambda 1037$ .

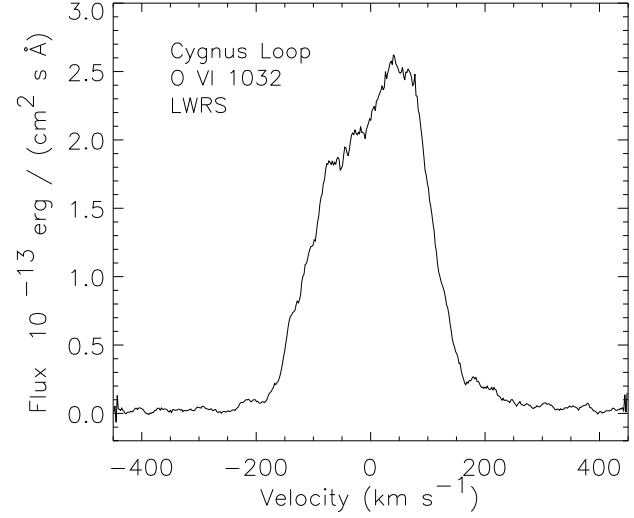


Figure 3: O VI  $\lambda 1032$  profile for the total nighttime exposure of all four positions for the LWRS.

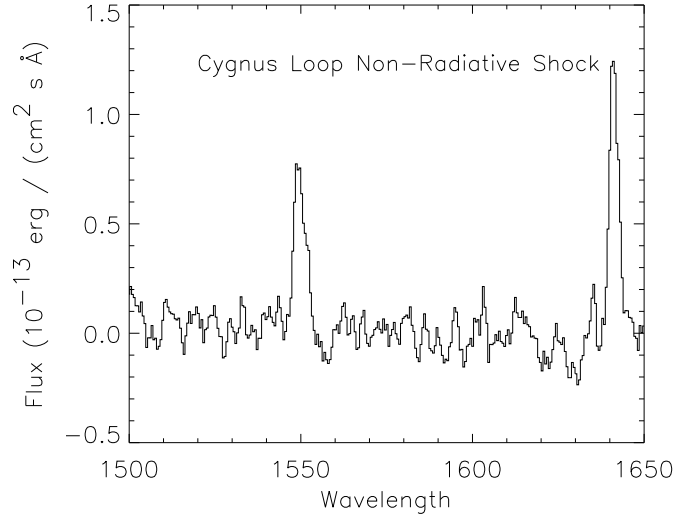


Figure 4: HUT spectrum showing the wavelength range including C IV  $\lambda\lambda 1548, 1550$  and He II  $\lambda 1640$ .

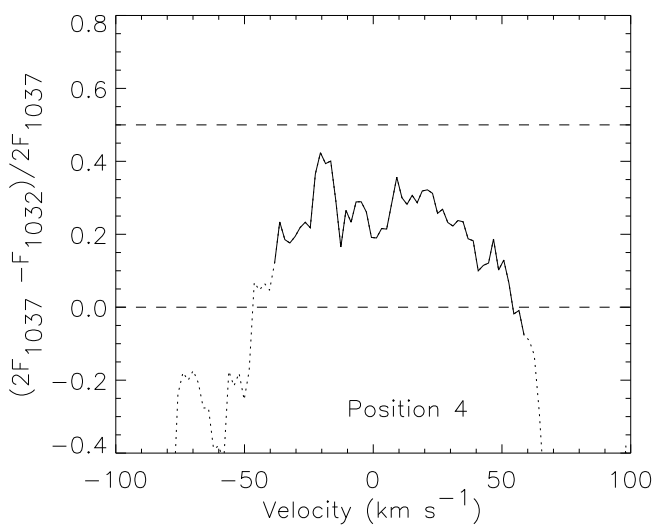
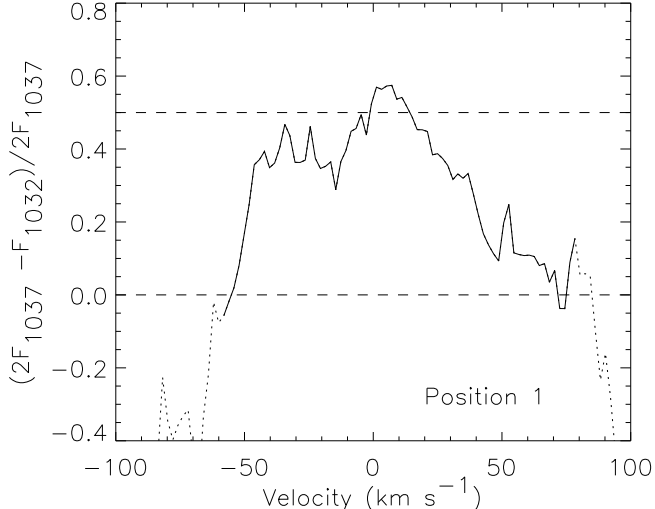


Figure 5 –(a) The intensity ratio of Equation 2 for Position 1. Dotted line indicates velocity range where absorption by C II or H<sub>2</sub> affects the ratio. (b) Same for Position 4.

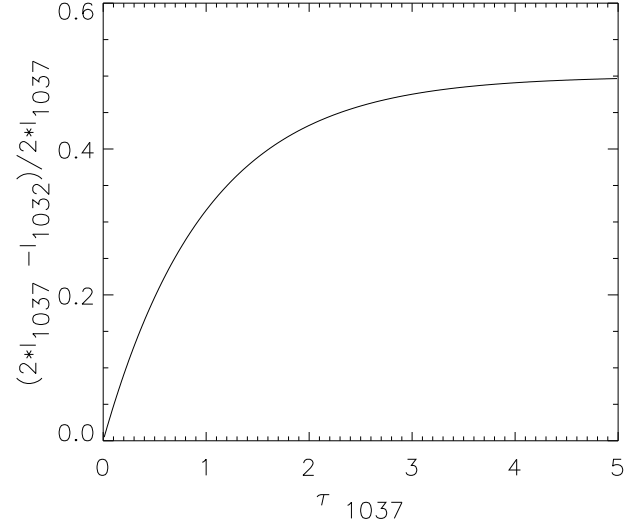


Figure 6: Theoretical value of the intensity ratio R plotted against  $\tau_{1037}$ .

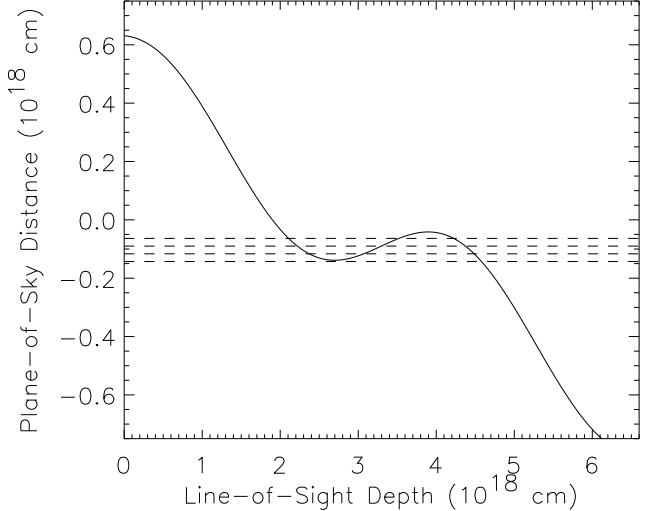


Figure 7: Shape of the emitting sheet along the line of sight. Note that the X-scale is compressed by a factor of 5 compared with the Y scale. Dashed lines indicate the lines of sight for the 4 FUSE MDRS spectra.

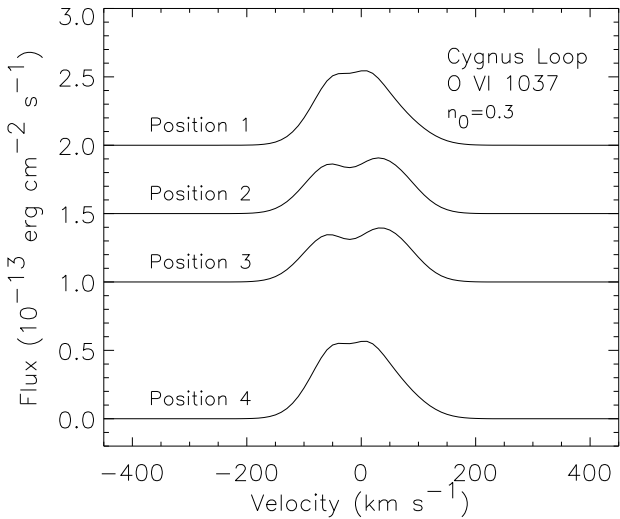
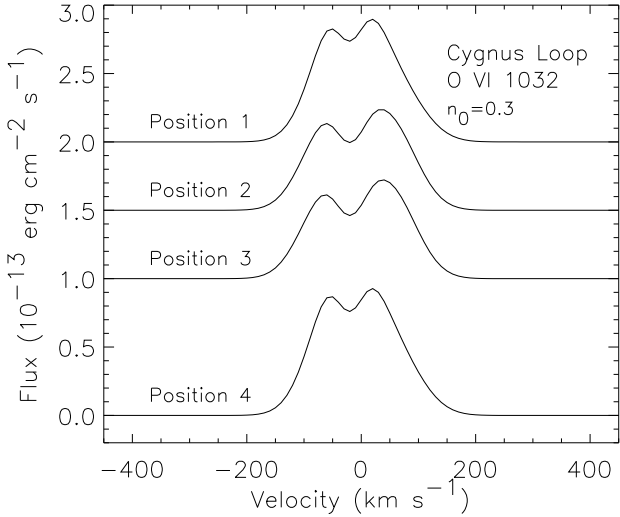


Figure 8 –(a) Predicted O VI  $\lambda 1032$  line profiles for the four MDRS spectra for a  $350 \text{ km s}^{-1}$  shock with the shape of Figure 7 and a pre-shock density of  $0.5 \text{ cm}^{-3}$ . (8b) Same for O VI  $\lambda 1037$ .

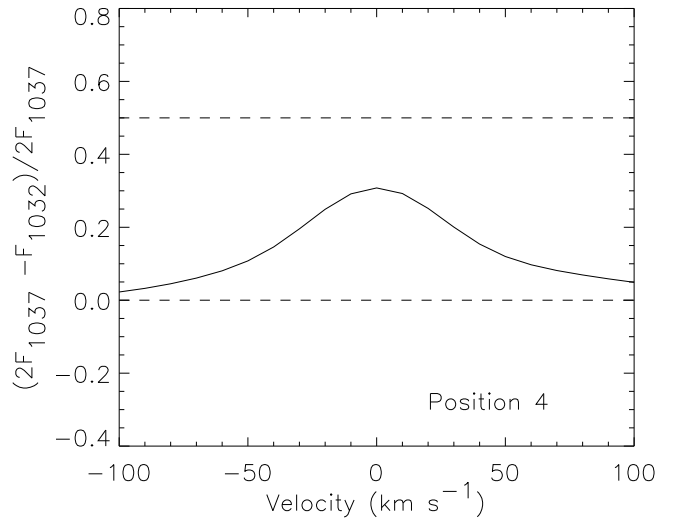
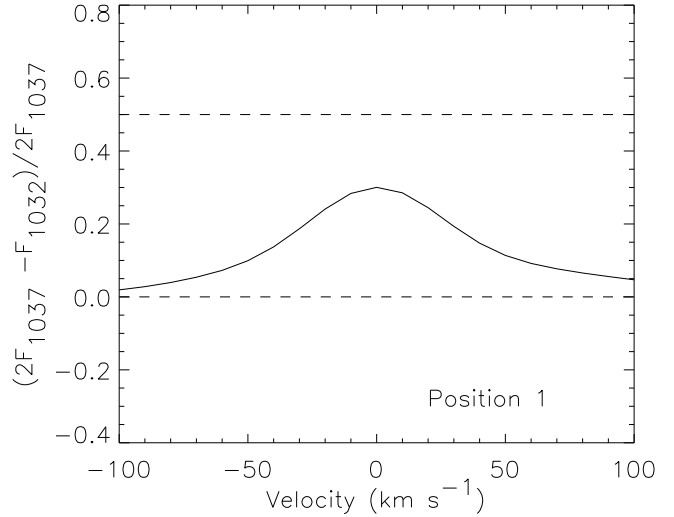


Figure 9 –(a) Predicted intensity ratios corresponding to Figure 5a for position 1. (b) Predicted intensity ratios corresponding to Figure 5b for position 4.

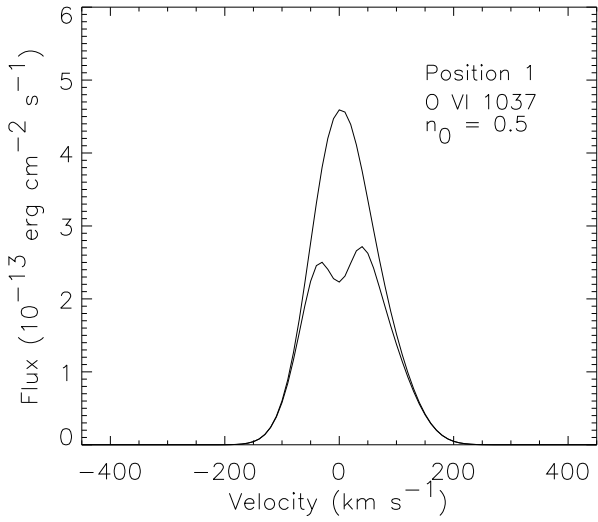


Figure 10: O VI  $\lambda 1032$  profile for the optically thin case and including the effects of interstellar and intrinsic resonance scattering. Interstellar reddening will reduce the fluxes by about a factor of 2.8.

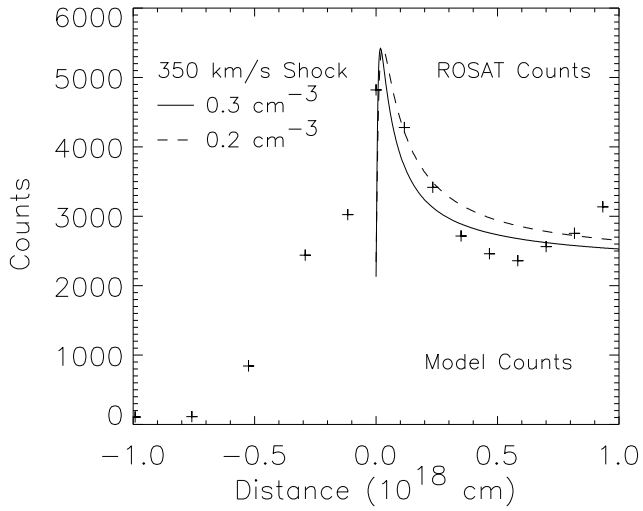


Figure 11: Predicted ROSAT PSPC count rates as a function of distance behind the H $\alpha$  filament, along with measured values (+).